

Field inversion for data-augmented RANS modelling in turbomachinery flows

*Original*

Field inversion for data-augmented RANS modelling in turbomachinery flows / Ferrero, A.; Iollo, A.; Larocca, F.. - In: COMPUTERS & FLUIDS. - ISSN 0045-7930. - ELETTRONICO. - 201:(2020), p. 104474.  
[10.1016/j.compfluid.2020.104474]

*Availability:*

This version is available at: 11583/2803272 since: 2020-03-23T11:09:47Z

*Publisher:*

Elsevier Ltd

*Published*

DOI:10.1016/j.compfluid.2020.104474

*Terms of use:*

This article is made available under terms and conditions as specified in the corresponding bibliographic description in the repository

*Publisher copyright*

Elsevier postprint/Author's Accepted Manuscript

© 2020. This manuscript version is made available under the CC-BY-NC-ND 4.0 license  
<http://creativecommons.org/licenses/by-nc-nd/4.0/>. The final authenticated version is available online at:  
<http://dx.doi.org/10.1016/j.compfluid.2020.104474>

(Article begins on next page)

This is a pre-print version.

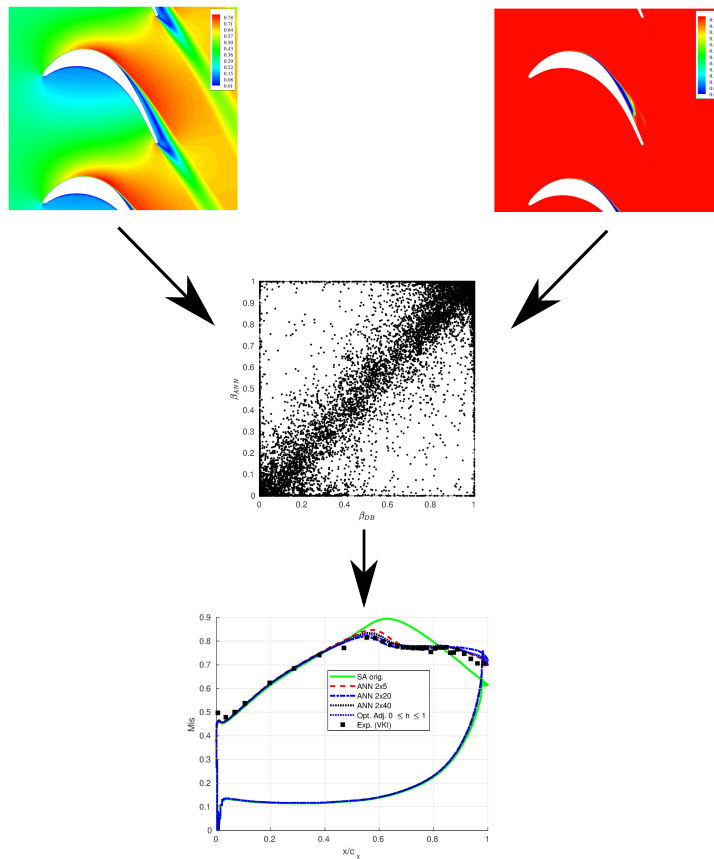
The final version is available at:

<https://doi.org/10.1016/j.compfluid.2020.104474>

# Graphical Abstract

## Field inversion for data-augmented RANS modelling in turbomachinery flows

Andrea Ferrero, Angelo Iollo, Francesco Larocca



## Highlights

- The field inversion approach is investigated for improving RANS models in turbomachinery flows
- Working conditions characterised by transition and separation are considered
- Some approaches to improve the robustness of the method are proposed
- The predictive ability of the method is investigated for several working conditions on different geometries

# Field inversion for data-augmented RANS modelling in turbomachinery flows

Andrea Ferrero<sup>a,\*</sup>, Angelo Iollo<sup>b,c,d</sup>, Francesco Larocca<sup>a</sup>

<sup>a</sup>*Politecnico di Torino, 10129 Torino, Italy*

<sup>b</sup>*Memphis Team, INRIA, F-33400 Talence, France*

<sup>c</sup>*Univ. Bordeaux, IMB, UMR 5251, F-33400 Talence, France*

<sup>d</sup>*CNRS, IMB, UMR 5251, F-33400 Talence, France*

---

## Abstract

Turbulence modelling in turbomachinery flows remains a challenge, especially when transition and separation phenomena occur. Recently, several research efforts have been devoted to the improvement of closure models for Reynolds Averaged Navier-Stokes (RANS) equations by means of machine learning approaches which make it possible to extract the knowledge hidden inside the available high-fidelity data (from experiments or from scale-resolving simulations). In this work the use of the field inversion approach is investigated for the augmentation of the Spalart-Allmaras RANS model applied to the flow in low pressure gas turbine cascades. As a first step, the field inversion method is applied to the T106c cascade at two different values of Reynolds number (80000-250000): an adjoint-based gradient method is employed in order to minimise the prediction error on the wall isentropic Mach number distribution. The data obtained by the correction field are then analysed by means of an Artificial Neural Network (ANN) which makes it possible to

---

\*Corresponding author

*Email address:* [andrea\\_ferrero@polito.it](mailto:andrea_ferrero@polito.it) (Andrea Ferrero)

generalise the correction by finding correlations which depend on physical variables. A study on the definition of the input variables and on the architecture of the ANN is performed. Different kind of corrections are evaluated and a particularly robust correction factor is obtained by limiting the range of the correction in the spirit of intermittency models. Finally, the ANN is introduced in an augmented version of the Spalart-Allmaras model which is tested on the T106c cascade (for values of the Reynolds number not considered during the training) and for the T2 cascade. The prediction ability of the method is investigated by comparing the numerical predictions with the available experimental data not only in terms of wall isentropic Mach number distribution (which was used as goal function during the field inversion) but also in terms of mass averaged exit angle and kinetic losses.

*Keywords:* Field inversion, Machine learning, Turbulence modelling, Turbomachinery

---

## 1. Introduction

The recent trends in the simulation of the flow field inside aerospace propulsion systems are characterised by a growing interest towards high-fidelity simulations which have become feasible thanks to a significant increase in the available computational power. This paves the way to the possibility of understanding complex physical effects which characterise turbulence and combustion phenomena in modern engines. The ability to understand and control these effects can be exploited to increasing the performance and reduce the emissions of existing propulsion systems. However, scale-resolving simulations (like for example Direct Numerical Sim-

11 ulations (DNS) or Large Eddy Simulations (LES)) cannot be easily integrated  
12 in the design process of industrial components. This is due to two main rea-  
13 sons: computational cost and difficulty to manage the results. It is clear  
14 that in the first steps of a design process several configurations must be in-  
15 vestigated and the use of high-fidelity simulations in this phase would have a  
16 prohibitive cost. For this reason, less expensive approaches like RANS equa-  
17 tions will be probably used for several years. As far as the management of the  
18 results is concerned, LES and DNS usually generate a huge amount of data  
19 for each simulation: in order to extract the useful information required by the  
20 design process it would be necessary to perform a complex post-process step.  
21 For example, even the computation of the average field from unsteady DNS  
22 data is not trivial because it is not known a-priori the extension of the time  
23 window required to get statistically converged results: several examples of  
24 low frequency phenomena which make difficult to compute the average field  
25 can be found in the literature, even looking to simple test cases, and special  
26 strategies to estimate the statistical error should be used (1). A review of  
27 the current state of the art for high-fidelity simulations in turbomachinery  
28 was proposed by Sandberg and Michelassi (2).

29

30 Recently, several research efforts have been devoted to the development  
31 of machine learning algorithms for all those applications in which a large  
32 amount of data must be processed. In particular, several recent works in the  
33 literature have been devoted to the use of machine learning techniques to  
34 analyse high-fidelity data from experiments or high-fidelity numerical simu-  
35 lations. The idea behind most of these recent works is to get the physical

36 insight hidden in the data and use it to develop or improve low order data-  
37 driven models. An example of this philosophy is represented by the work  
38 of Xie et al. (3) who proposed a filtered reduced order model with a data-  
39 driven closure. Dupuis et al.(4) proposed an approach in which traditional  
40 surrogate models and machine learning are combined to improve the predic-  
41 tion of the flow on airfoils which work in subsonic or transonic conditions.  
42 Margheri et al.(5) performed a study on the epistemic uncertainty of some  
43 popular RANS models and used a generalised Polynomial Chaos response  
44 surface to perform the calibration of the model coefficients in the spirit of  
45 data assimilation strategies. In (6) the Proper Orthogonal Decomposition  
46 approach is used in a discontinuous Galerkin (DG) finite element framework  
47 (7) together with a domain decomposition strategy (8) to learn empirical  
48 local bases which are used to reduce the simulation cost of the flow field in  
49 gas turbines.

50 An alternative path was followed by Raissi and Karniadakis (9) who pro-  
51 posed an approach to identify the partial differential equations which govern  
52 a set of data: they applied the algorithm to an example in which they recov-  
53 ered the Navier-Stokes equations used to generate the database but the same  
54 approach could be used on experimental data to recover turbulence models.  
55 While the work of Raiss and Karniadakis (9) aims at discovering the full  
56 governing model, several works focus on the improvement of existing models.  
57 For example, Wang et al. (10) developed a machine learning strategy to pre-  
58 dict the discrepancy in RANS modelled Reynolds stresses starting from DNS  
59 data. Weatheritt et al.(11) proposed the use of Gene Expression Program-  
60 ming to identify new expressions for the stress-strain relationship. Promising



61 results were obtained with this technique on high pressure turbines (12).  
62 Duraisamy et al. (13; 14) proposed a strategy based on field inversion and  
63 machine learning which allows to improve the prediction ability of RANS  
64 models. This approach is exploited in the present work in order to improve  
65 RANS modelling for low pressure gas turbine cascades.  
66 Machine learning techniques have been investigated also on multiphase flows  
67 (15; 16), combustion (17; 18; 19) and engine modelling (20; 21). Finally, a  
68 comprehensive review of the machine learning techniques proposed for the  
69 improvement of turbulence modelling can be found in (22).  
70 The paper is organised as follows. In Section 2 the original RANS model is  
71 presented. In Section 3 the methods used for the discretisation of the equa-  
72 tions are described. In Section 4 the field inversion approach is described and  
73 it is then applied to the T106c gas turbine cascade in Section 5. The data  
74 obtained by the field inversion are analysed by means of machine learning  
75 techniques in Section 6 in order to generalise the obtained results. Finally,  
76 the improved RANS model is tested on the T106c and on the T2 cascades in  
77 Section 7.

## 78 **2. Physical model**

79 This work is devoted to the prediction of the compressible turbulent flow  
80 in 2D turbine cascades. The study starts from the Spalart-Allmaras (SA)  
81 model implemented for compressible equations, following the guidelines of  
82 (23). This model is widely used in the literature for fully turbulent flows.  
83 However, the model is not suitable for the prediction of transitional flows at  
84 low Reynolds numbers. The original model gives the possibility to impose

85 the transition location (by means of the trip term  $f_{t1}$  defined in (23)) but this  
 86 choice is rarely followed in the literature because in general the location of  
 87 transition is not known a-priori. Furthermore, when the transition trip term  
 88  $f_{t1}$  is used a second term  $f_{t2}$  for delaying natural transition (and making the  
 89 trip term  $f_{t1}$  effective) is also activated. Further details on the effects of the  
 90 term  $f_{t2}$  in the prediction of the flow around the T106c cascade can be found  
 91 in (24).

92 In the present work the SA model is used without the trip terms  $f_{t1}$  and  
 93  $f_{t2}$ . With this choice the model is expected to work fine for high Reynolds  
 94 numbers but to fail in predicting transition and separation at low values of  
 95 Reynolds number. This model tends indeed to produce an excessive amount  
 96 of turbulent eddy viscosity on this kind of flows (24). For this reason, it  
 97 represents an optimal baseline for testing the field inversion approach and  
 98 evaluating how much the original model can be improved.

99 The mass-averaged RANS equations are reported in the following:

$$\frac{\partial \rho}{\partial t} + \nabla \cdot (\rho \mathbf{u}) = 0 \quad (1)$$

$$\frac{\partial}{\partial t}(\rho \mathbf{u}) + \nabla \cdot (\rho \mathbf{u} \mathbf{u}) = -\nabla p + \nabla \cdot \boldsymbol{\tau} \quad (2)$$

$$\frac{\partial E}{\partial t} + \nabla \cdot (\mathbf{u}(E + p)) = \nabla \cdot (\boldsymbol{\tau} \cdot \mathbf{u} - \mathbf{q}) \quad (3)$$

$$\frac{\partial \rho \hat{\nu}}{\partial t} + \nabla \cdot (\rho \mathbf{u} \hat{\nu}) = \rho(P - D) + \frac{1}{\sigma} \nabla \cdot (\rho(\nu + \hat{\nu}) \nabla \hat{\nu}) + \frac{c_{b2}}{\sigma} \rho (\nabla \hat{\nu})^2 - \frac{1}{\sigma} (\nu + \hat{\nu}) \nabla \rho \cdot \nabla \hat{\nu} \quad (4)$$

100 where  $\rho$ ,  $\mathbf{u}$ ,  $p$ ,  $E$ ,  $\nu$ ,  $\hat{\nu}$ ,  $\mathbf{x}$  and  $t$  are density, velocity, pressure, total  
 101 energy per unit volume, molecular viscosity, modified eddy viscosity, spatial  
 102 position and time, respectively. A fluid with constant specific heat ratio  $\gamma$   
 103 and constant viscosity is considered. The following equation for the energy  
 104 is considered:

$$E = \frac{P}{\gamma - 1} + \frac{1}{2}\rho\mathbf{u} \cdot \mathbf{u} \quad (5)$$

105 where  $\gamma$  is the specific heat ratio.

106 The viscous stress tensor  $\boldsymbol{\tau}$  includes both the molecular and eddy viscosity  
 107 contributions and its components are given by:

$$\tau_{ij} = 2\rho(\nu + \hat{\nu}f_{v1}) \left( \frac{1}{2} \left( \frac{\partial u_i}{\partial x_j} + \frac{\partial u_j}{\partial x_i} \right) - \frac{1}{3} \frac{\partial u_k}{\partial x_k} \delta_{ij} \right) \quad (6)$$

108 The production  $P$  and destruction  $D$  terms in Eq. 4 are computed as follows:

$$P = c_{b1}\tilde{S}\tilde{\nu} \quad D = c_{w1}f_w \left( \frac{\tilde{\nu}}{\bar{d}} \right)^2 \quad (7)$$

109 with the following definitions:

$$f_w = g \left( \frac{1 + c_{w3}^6}{g^6 + c_{w3}^6} \right)^{1/6} \quad g = r + c_{w2}(r^6 - r) \quad r = \min \left( \frac{\tilde{\nu}}{\tilde{S}^2\kappa^2 d^2}, r_{lim} \right) \quad (8)$$

$$\tilde{S} = \begin{cases} S + \bar{S} & \text{if } \bar{S} \geq -c_{v2}S \\ S + \frac{S(c_{v2}^2 S + c_{v3}\bar{S})}{(c_{v3} - 2c_{v2})S - \bar{S}} & \text{if } \bar{S} < -c_{v2}S \end{cases} \quad (9)$$

110 where  $S$  is the vorticity magnitude and  $\bar{S}$  is:

$$\bar{S} = \frac{\tilde{\nu}}{\kappa^2 d^2} f_{v2} \quad (10)$$

111 The functions  $f_{v1}$  and  $f_{v2}$  depend on the viscosity ratio  $\chi = \frac{\tilde{\nu}}{\nu}$ :

$$f_{v1} = \frac{\chi^3}{\chi^3 + c_{v1}^3} \quad f_{v2} = 1 - \frac{\chi}{1 + \chi f_{v1}} \quad (11)$$

112 The constants  $\sigma$ ,  $c_{b1}$ ,  $c_{b2}$ ,  $c_{v1}$ ,  $c_{w1}$  are defined in (23).

113 Finally, the heat flux  $\mathbf{q}$  is described by the Fourier's law:

$$\mathbf{q} = - \left( \frac{c_p \mu}{Pr} + \frac{c_p \rho \hat{\nu} f_{v1}}{Pr_t} \right) \nabla T \quad (12)$$

114 where  $T$ ,  $c_p$ ,  $Pr$  and  $Pr_t$  are the temperature, the constant pressure specific  
115 heat capacity, the Prandtl number and the turbulent Prandtl number. The  
116 test cases considered in this work refer to experiments performed with air  
117 and so the following values are assumed:  $\gamma = 1.4$ ,  $Pr = 0.72$  and  $Pr_t = 0.9$ .

118

### 119 **3. Implicit Discontinuous Galerkin discretization**

120 The discontinuous Galerkin (DG) scheme is used in this work for the  
121 spatial discretisation on the governing equations. This approach is charac-  
122 terised by a significant flexibility since it allows to easily manage high-order  
123 reconstructions on unstructured meshes. The main idea behind this kind of  
124 scheme consists in adopting an high-order polynomial reconstruction inside  
125 each element without any continuity constraint at the interface between dif-  
126 ferent elements. As a result, the scheme can be easily exploited in the frame-  
127 work of automatic adaptive approaches, in which both the size (h-adaptivity,  
128 (25; 26; 27; 28)), the order (p-adaptivity (29; 30; 31)) or both properties  
129 (hp-adaptivity, (32; 33; 34)) can be locally adapted following some error in-  
130 dicators.

131

132 The computational domain  $\Omega$  is discretised with a hybrid mesh which  
133 contains a structured boundary layer mesh close to the body surrounded

134 by an unstructured mesh. The grid is generated by means of Gmsh (35)  
 135 with the Frontal-Delaunay for Quads algorithm. The management of the  
 136 unstructured grid in the parallel MPI environment is performed through the  
 137 DMPlex class (36) provided by the PETSc library (37).

138 The numerical approximation of the  $l$ -th conservative variable  $u_l(\mathbf{x}, t)$  inside  
 139 each element  $\Omega_e$  is described by a modal basis with size  $N_e = \frac{(k+1)(k+2)}{2}$  with  
 140 a reconstruction order  $k$ :

$$u_l(\mathbf{x}, t) = \sum_{i=1}^{N_e} \tilde{u}_{li}(t) \phi_i(\mathbf{x}) \quad 1 \leq i \leq N_e \quad (13)$$

141 where  $\tilde{u}_{li}(t) \in \mathbb{R}^{N_e}$  contains the degrees of freedom inside the element for  
 142 the  $l$ -th conservative variable. The basis functions  $\phi_i(\mathbf{x})$  are obtained by the  
 143 modified Gram-Schmidt orthonormalisation applied to a set of monomials  
 144 defined in the physical space, following the approach of Bassi et al. (38). In  
 145 this work a third order accurate DG scheme is used ( $k = 2$ ,  $N_e = 6$ ).

146 The spatial discretisation is completed by a projection of the governing equa-  
 147 tion on the space of the approximation functions. The resulting weak formu-  
 148 lation consists in a set of ordinary differential equations in time. The con-  
 149 vective terms which appear in the numerical fluxes at the interface between  
 150 the elements are evaluated by means of an approximate Riemann problem  
 151 solver (following (39) and (40)). Diffusive terms are evaluated by means of  
 152 a recovery-based approach (41).

153 Time integration is here performed by means of the linearised implicit  
 154 Euler method. Since steady problems are considered the use of a first order  
 155 time integrator appears suitable since it does not influence the accuracy of the  
 156 final steady solution and it has good dissipative properties which are useful to  
 157 accelerate the numerical transients. The solution of the linear system which

158 is obtained at each time step is performed in parallel by means of the GMRES  
159 algorithm with the additive Schwarz preconditioner provided by the PETSc  
160 library (37). The GMRES algorithm is employed by setting the maximum  
161 number of iterations to 200, the dimension of the Krylov subspace to 100 and  
162 the absolute tolerance to  $10^{-12}$ . The CFL number which controls the time  
163 step size is automatically adjusted according to the evolution of the residuals  
164 following the pseudo-transient continuation strategy (42). In particular, the  
165 CFL number is allowed to vary between  $10^2$  and  $10^4$ . During the first steps  
166 of the transient, a feedback filtering procedure (43) is applied to remove  
167 potential instabilities which can appear due to the large CFL number. This  
168 filtering procedure is deactivated when the residuals drop under a certain  
169 threshold and so it does not influence the steady solution.

#### 170 4. Field inversion and machine learning in a DG framework

171 The field inversion approach proposed by (14) requires to define a goal  
172 function  $G$  which measures the distance between the experimental data and  
173 the predicted numerical results. The procedure requires the solution of an  
174 optimisation problem in which a field  $\beta(x)$  is found in order to minimise  
175 the goal function  $G$ . The field  $\beta(x)$  is then introduced in a correction term  
176  $h(\beta(x))$  which multiplies the production term in the SA transport equation:

$$\frac{\partial \rho \hat{\nu}}{\partial t} + \nabla \cdot (\rho \mathbf{u} \hat{\nu}) = \rho [h(\beta)P - D] + \frac{1}{\sigma} \nabla \cdot (\rho(\nu + \hat{\nu}) \nabla \hat{\nu}) + \frac{c_{b2}}{\sigma} \rho (\nabla \hat{\nu})^2 - \frac{1}{\sigma} (\nu + \hat{\nu}) \nabla \rho \cdot \nabla \hat{\nu} \quad (14)$$

177 In the original works of (14; 44) the correction was chosen as  $h(\beta) = \beta$ . In  
178 this work, different choices are investigated for the function  $h(\beta)$ , as described

179 in the next section.

180 As far as the goal function  $G$  is concerned, the following choice is made:

$$G = \int_w (M_s - M_s^{exp})^2 dl + \lambda \int_{\Omega} (\beta - 1)^2 d\Omega \quad (15)$$

181 The first term is a line integral performed on the wall of the blade and allows  
182 to evaluate the norm-2 error on the wall isentropic Mach number distribution  
183  $M_s$ , which is defined as:

$$M_s = \sqrt{\frac{2}{\gamma - 1} [(p_i^0/p_w)^{(\gamma-1)/\gamma} - 1]} \quad (16)$$

184 where  $p_w$  is the static pressure at wall and  $p_i^0$  is the inlet total pressure.

185 The second term is a surface integral on the computational domain  $\Omega$  which  
186 acts as a Tikhonov regularisation (45): it penalises the goal function when  
187 the correction factor is far from 1. This is useful to avoid unnecessary correc-  
188 tions which could be introduced during the optimisation process but which  
189 are not required in the final optimal solution. The choice of the penalisation  
190 constant  $\lambda$  will be discussed in the next Section.

191

192 In order to solve the optimisation problem, a simple gradient descent  
193 method is applied. The field  $\beta$  will be described in terms of the same basis  
194 functions used for the conservative variables. Starting from the original SA  
195 model ( $h(\beta(x)) = 1$ ) the degrees of freedom related to the field  $\beta$  are updated  
196 with the gradient descent method:

$$\tilde{\beta} = \beta - \delta \frac{dG}{d\beta} \quad (17)$$

197 where  $\delta$  is the step size that in this work is chosen constant for simplicity  
198 ( $\delta = 0.1$ ).

199 Since the dimension of the optimisation problem is related to the total num-  
 200 ber of degrees of freedom per equation the computation of the gradient  $\frac{dG}{d\tilde{\beta}}$   
 201 by means of numerical differentiation would be prohibitive. For this reason,  
 202 an adjoint-based gradient evaluation was implemented. The gradient of the  
 203 goal function  $G$  which respect to the degrees of freedom of the field  $\beta(x)$  is  
 204 computed as:

$$\frac{dG}{d\tilde{\beta}} = \frac{\partial G}{\partial \tilde{\beta}} + \psi^T \frac{\partial R}{\partial \tilde{\beta}} \quad (18)$$

205 where  $R$  represents the residual of the governing equations. The first term  
 206 contains only the contributions related to the penalisation integral which  
 207 appears in the goal function. The adjoint variable  $\Psi$  is computed by the  
 208 solution of the following linear system with the GMRES iterative solver:

$$\left[ \frac{\partial R}{\partial \tilde{u}} \right]^T \Psi = - \left[ \frac{\partial G}{\partial \tilde{u}} \right]^T \quad (19)$$

209 in which the jacobian matrix  $\left[ \frac{\partial R}{\partial \tilde{u}} \right]$  is already available from the implicit time  
 210 integrator and the term  $\left[ \frac{\partial G}{\partial \tilde{u}} \right]$  contains the derivatives of the goal function  
 211 with respect to the fluid dynamics degrees of freedom. This last term was  
 212 computed by means of automatic differentiation with the Tapenade tool (46).  
 213 Summarising, the procedure works as follows. First of all, a steady solution  
 214 with the original SA model is obtained. The solution is considered steady  
 215 when the residuals of all the governing equations are lower than  $10^{-6}$ . Usua-  
 216 lly, the SA equation is the one which converges with the lowest speed so  
 217 when the condition is satisfied the residuals of the Eqs. 1-3 are orders of  
 218 magnitudes lower (typically around  $10^{-8}$ - $10^{-10}$ ). When the steady solution  
 219 is reached, the gradient  $\frac{dG}{d\tilde{\beta}}$  is computed by the adjoint approach and the  
 220 correction field is updated. This generates a transient which is solved in



221 time up to a new steady solution. Since the perturbation introduced by the  
222 correction update is small, the transient can be easily solved by marching in  
223 time with a very large CFL number. For example, in this work the constant  
224 value CFL=5000 is used for this part of the computation. The procedure is  
225 repeated until the goal function does not show any significant improvement.

226

227 The correction field  $h(\beta(x))$  obtained by the inversion process can be  
228 exploited for different purposes. On one hand, it gives insight for the devel-  
229 opment of new turbulence models since it shows where and how the original  
230 model fails. On the other hand, it is possible to directly generalise the cor-  
231 rection in order to obtain a new model which can be used for predictive  
232 simulations. For example, Duraisamy and Durbin (47) used the results of  
233 field inversion to define a transport equation for an intermittency factor,  
234 where the different terms of the transport equation are computed by means  
235 of machine learning techniques. Alternatively, it is possible to find a local  
236 closure which allows to define the correction field as a function of local phys-  
237 ical quantities (14; 44). This last approach is followed in the present work.  
238 In particular, the results of the inverse problem will be exploited to train  
239 an Artificial Neural Network (ANN) which can then be used to define an  
240 augmented version of the SA model.

## 241 **5. Field inversion on the T106c cascade**

242 The field inversion approach is here applied to the flow around the T106c  
243 gas turbine cascade. This profile is representative of high-lift low pressure  
244 gas turbines in modern turbofan engines. The cascade was experimentally

245 investigated at the VKI and some experimental results are available from  
246 the literature (48; 49; 50). In particular, the wall isentropic Mach number  
247 distribution, the mass averaged kinetic losses and exit angle in the wake are  
248 available for several values of the Reynolds number. The flow field is studied  
249 for an inlet angle  $\alpha = 32.7^\circ$ , an isentropic exit Mach number  $M_{2s} = 0.65$   
250 and different values of the exit isentropic Reynolds number  $8 \cdot 10^4 \leq Re_{2s} \leq$   
251  $2.5 \cdot 10^5$ . The Reynolds number  $Re_{2s}$  is defined by using the blade chord and  
252 the isentropic exit velocity and density. The dynamic viscosity is assumed  
253 constant. The turbulence intensity during the experiments was very low  
254 (0.9%): for this reason all the RANS simulations are performed by setting a  
255 very small value of inlet eddy viscosity ( $\tilde{\nu}/\nu = 0.1$ ).

256 Houmorziadis (51) showed that the Reynolds number in low pressure gas  
257 turbines of turbofan engines is the range between  $10^5 - 4 \cdot 10^5$  where the  
258 smaller values are observed in cruise conditions and the higher values are  
259 obtained at take-off. The high-lift profiles can show large laminar separations  
260 at low values of Reynolds number. When the Reynolds number is increased  
261 the separation transforms from an open separation to a closed separation in  
262 which there is a separation bubble followed by reattached flow. The evolution  
263 from one configuration to the other takes place in a small range of Reynolds  
264 number and so the flow is quite sensitive to the working condition.

265 The presence of separation can be easily noticed in the experimental studies  
266 on these flows by checking the wall isentropic Mach number distribution: the  
267 separation is usually related to the presence of a plateau in the distribution.  
268 Singh et al.(44) showed that the wall pressure distribution (which is directly  
269 related to the isentropic Mach number distribution) can be effectively used

270 in the field inversion approach for improving the prediction of separated  
 271 flows. They indeed showed that the field inversion based on the wall pressure  
 272 distribution can significantly improve the prediction of the Reynolds stresses  
 273 in the separation region (44). For these reasons, the field inversion algorithm  
 274 used in this work will use the error on the wall isentropic Mach number  
 275 distribution as goal function.

276 First of all, a convergence study is performed on the T106c cascade with the  
 277 original SA model at the highest Reynolds number ( $Re_{2s} = 2.5 \cdot 10^5$ ). Three  
 278 different meshes and two reconstruction orders ( $1 \leq k \leq 2$ ) are evaluated.  
 279 The convergence level is assessed by checking the mass averaged value of the  
 280 kinetic losses in a control section located  $0.465c_x$  behind the trailing edge.  
 281 The kinetic losses are defined in the following way:

$$\zeta = 1 - \frac{1 - (p_e/p_e^0)^{(\gamma-1)/\gamma}}{1 - (p_e/p_i^0)^{(\gamma-1)/\gamma}} \quad (20)$$

282 where  $p_e$ ,  $p_e^0$  and  $p_i^0$  are the static pressure in the control section, the total  
 283 pressure in the control section and the inlet total pressure, respectively. The  
 284 results of the convergence analysis are reported in Table 1 which shows the  
 285 number of elements  $n_{ele}$ , the number of degrees of freedom per equation  
 286  $n_{DOF}$  and the predicted averaged losses. It is useful to remember that in the  
 287 asymptotic range mesh refinement gives a fixed convergence order (depending  
 288 on  $k$ ) while order refinement gives exponential convergence.

289 We emphasise that the losses in the wake represent a better goal function for  
 290 the convergence assessment with respect to the wall isentropic Mach number  
 291 distribution because the original SA model over-predicts significantly the  
 292 turbulence eddy viscosity and so it gives a wall isentropic Mach number  
 293 distribution which is very similar to what would be obtained by an inviscid

294 Euler simulation, regardless of the mesh resolution. In contrast, the wake  
 295 losses are influenced by the mesh resolution in the boundary layer and in the  
 296 wake region.

297 The mesh C reported in Tab.1 will be used for all the following simulations  
 298 with a third order accurate DG scheme ( $k = 2$ ). The mesh contains 40436  
 299 elements and so the total number of degrees of freedom per equation is equal  
 300 to 242616. The dimensionless wall cell size is  $y^+ < 1$  on the entire surface.

	$n_{ele}$	$n_{DOF}$	$\zeta$
Mesh A, k=1	11480	34440	2.39E-002
Mesh B, k=1	21195	63585	2.27E-002
Mesh C, k=1	40436	121308	2.24E-002
Mesh A, k=2	11480	68880	2.25E-002
Mesh B, k=2	21195	127170	2.24E-002
Mesh C, k=2	40436	242616	2.24E-002

Table 1: Mass averaged kinetic losses: convergence with grid size and reconstruction order

301 As reported in Equation 14, the field inversion approach requires to alter  
 302 the production term by the presence of the correction factor  $h(\beta)$ . In this  
 303 work, different expressions for  $h(\beta)$  are investigated. The most straightfor-  
 304 ward approach, which was used by Singh et al. (44) for the study of wind  
 305 turbine airfoils, consists in setting :

$$h(\beta) = \beta \quad \beta \in \mathbb{R} \quad (21)$$

306 In this way the correction factor is free to assume both positive and negative  
 307 values and so the correction term is very general. However, this generality

308 comes with a price: since  $h(\beta)$  is not limited it can lead to unstable numerical  
 309 results during the transients which must be solved in predictive simulations.  
 310 An alternative approach, experimented in this work, consists in setting

$$h(\beta) = \beta^2 \quad \beta \in \mathbb{R} \quad (22)$$

311 In this way the correction term is not allowed to assume negative values.  
 312 This means that the generality of the approach is reduced but the robust-  
 313 ness of the simulation is increased because the correction term cannot change  
 314 the nature of the production term (it can, in the limit, set the production  
 315 to zero but it cannot transform the production term into a destruction term).

316  
 317 A third approach, which showed the most robust results in this work,  
 318 is reported in the following. The idea behind this approach is to mimic  
 319 the behaviour of intermittency models in which the production term of the  
 320 RANS model is reduced by a factor defined in the range  $[0, 1]$  in order to  
 321 reproduce transition phenomena. Following this approach, the correction  
 322 term is defined as a smooth ramp function of  $\beta$ :

$$h(\beta) = \begin{cases} 0 & \text{if } \beta \leq 0 \\ 3\beta^2 - 2\beta^3 & \text{if } 0 < \beta < 1 \\ 1 & \text{if } \beta \geq 1 \end{cases} \quad (23)$$

323 This last approach is the least general between the three alternatives exam-  
 324 ined in this work but it is the most robust. This is due to the fact that,  
 325 in the end, the correction factor  $h$  will be expressed by means of an ANN.  
 326 When the SA model augmented by the ANN correction term will be used for

327 actual predictions, the ANN will be asked to compute the correction factor  
 328 for input values which could be outside of the range explored in the train-  
 329 ing database. This is very likely to happen during the numerical transient  
 330 which must be solved before getting the steady solution. However, ANNs  
 331 are known for their poor extrapolation accuracy and so the use of a more  
 332 general expression (like for example the one defined by Equation 21) would  
 333 allow the presence of unlimited values of the correction factor. In contrast,  
 334 when the correction factor is limited in the range  $0 \leq h \leq 1$  the model can  
 335 behave, in the limit, as the original SA model (when  $h \rightarrow 1$ ) or as the laminar  
 336 Navier-Stokes equations (when  $h \rightarrow 0$ ).

337

338 In order to understand whether the limitation introduced by Equation  
 339 23 affects the ability of the field inversion to match the experimental data,  
 340 the different definitions of  $h(\beta)$  are tested on the T106c cascade. In partic-  
 341 ular, the gradient based optimisation process is carried out for the T106c at  
 342  $Re_{2s} = 8 \cdot 10^4$  and  $Re_{2s} = 2.5 \cdot 10^5$ . The plot in Figure 1 shows the history  
 343 of the goal function during the optimisation process. The results shows that  
 344 after approximately 50 steps of the gradient descent algorithm a minimum  
 345 is reached. This optimisation is carried out by starting from the original SA  
 346 model with  $h = 1$  in all the domain and using the unlimited correction factor  
 347 defined by Eq. 21 with  $\lambda = 0$ .

348 The optimal field obtained from this first step is then used as initial field for  
 349 a second optimisation in which the correction factor is limited according to  
 350 Eq. 23. It is useful to emphasise that, in order to apply the correction factor  
 351 defined by Eq. 23, it is not possible to start with a uniform field with  $\beta = 1$ .

352 This is due to the fact that the derivative of the smooth ramp function is  
 353 null for  $\beta = 1$  and so it would not be possible to update the solution since  
 354 the gradient of the goal function would remain to zero according to Eq. 18  
 355 ( $\frac{\partial R}{\partial \beta} = \frac{\partial R}{\partial g} \frac{\partial g}{\partial \beta}$ , with  $\frac{\partial g}{\partial \beta} = 0$  for  $\beta = 1$ ).

356 In order to compare the two approaches, the wall isentropic Mach number  
 357 distribution is reported in Figure 2 for the original SA model and the op-  
 358 timised solutions related to Eq. 21 and 23. The results for the correction  
 359 factor defined by Eq.22 are not reported in the plot since they overlap the  
 360 other results related to 21 and 23. The Figure shows also the available exper-  
 361 imental data which are used to drive the optimisation process. The optimal  
 362 solutions show a good match with the experimental data and a significant  
 363 improvement with respect to the baseline model. This test confirms that  
 364 the limited correction factor defined by Eq. 23 is able to provide an optimal  
 365 solution which is comparable to the results provided by the unlimited correc-  
 366 tion factor. This is due to the fact that the original SA model overestimates  
 367 significantly the turbulence production in this kind of flows and so the use of  
 368 a correction factor limited between 0 and 1 is sufficient to correct the model.  
 369 In this sense, the correction factor proposed in this work acts exactly as a  
 370 intermittency correction in the framework of laminar-to-turbulence transi-  
 371 tion. After this analysis, the limited correction factor defined by Eq. 23 was  
 372 chosen for all the following simulations.

373 The plots in Figure 3 show the Mach field for the original SA model and  
 374 optimal model at  $Re_{2s} = 8 \cdot 10^4$  and  $Re_{2s} = 2.5 \cdot 10^5$ . The optimal solution at  
 375  $Re_{2s} = 8 \cdot 10^4$  is characterised by a large open separation which is completely  
 376 missed by the original SA model. The optimal solution at  $Re_{2s} = 2.5 \cdot 10^5$

377 shows a small separation bubble followed by reattachment. Again, this sep-  
378 aration is missed by the original SA model.

379 Finally, the correction field at  $Re_{2s} = 8 \cdot 10^4$  and  $Re_{2s} = 2.5 \cdot 10^5$  for the case  
380 defined by Eq. 23 is reported in Figures 4 and 5 for  $\lambda = 0$  and  $\lambda = 10^{-3}$ , re-  
381 spectively. An analysis of the pictures shows clearly that the adjoint approach  
382 obtained an optimal solution in which the production term is deactivated in  
383 the boundary layer for the first portion of the suction side: the algorithm  
384 has recovered a laminar separation just by using the knowledge on the ex-  
385 perimental wall isentropic Mach number distribution. As far as the influence  
386 of  $\lambda$  is concerned, a study with  $\lambda = 0, 10^{-2}, 10^{-3}, 10^{-4}$  is performed. These  
387 values are chosen by running a preliminary simulation with  $\lambda = 0$  and then  
388 evaluating the order of magnitude of the two integrals which appear in the  
389 goal function defined by Eq. 15. For all these values, the optimal wall isen-  
390 tropic Mach number distribution does not show significant variations. The  
391 weak influence of the parameter  $\lambda$  can be seen in Figures 4 and 5 where the  
392 higher value of  $\lambda$  tends to avoid unnecessary corrections at the end of the  
393 separation region.

394

## 395 **6. Machine learning on the T106c cascade**

396 The field inversion algorithm described in the previous section is able to  
397 provide a correction field which alters the original SA model in order to match  
398 very well the experimental results for two different working conditions. In  
399 this section this result will be generalised in order to express the correction  
400 factor as a function of some physical features. In particular, several choices



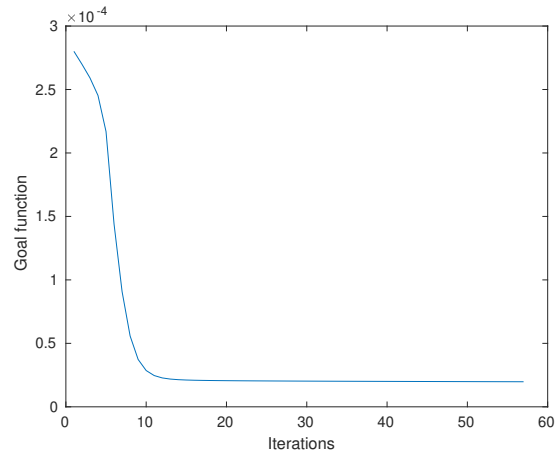


Figure 1: Adjoint-based optimization history for T106c at  $Re_{2s} = 8 \cdot 10^4$  with  $\beta \in R$

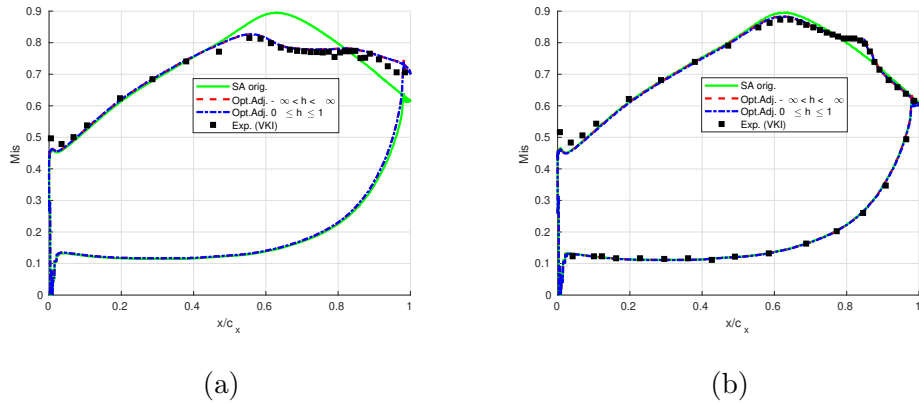


Figure 2: Comparison between original SA model, optimized model and experimental results in terms of  $Mis$  distribution for the T106c at  $Re_{2s} = 8 \cdot 10^4$  (a) and  $Re_{2s} = 2.5 \cdot 10^5$  (b)

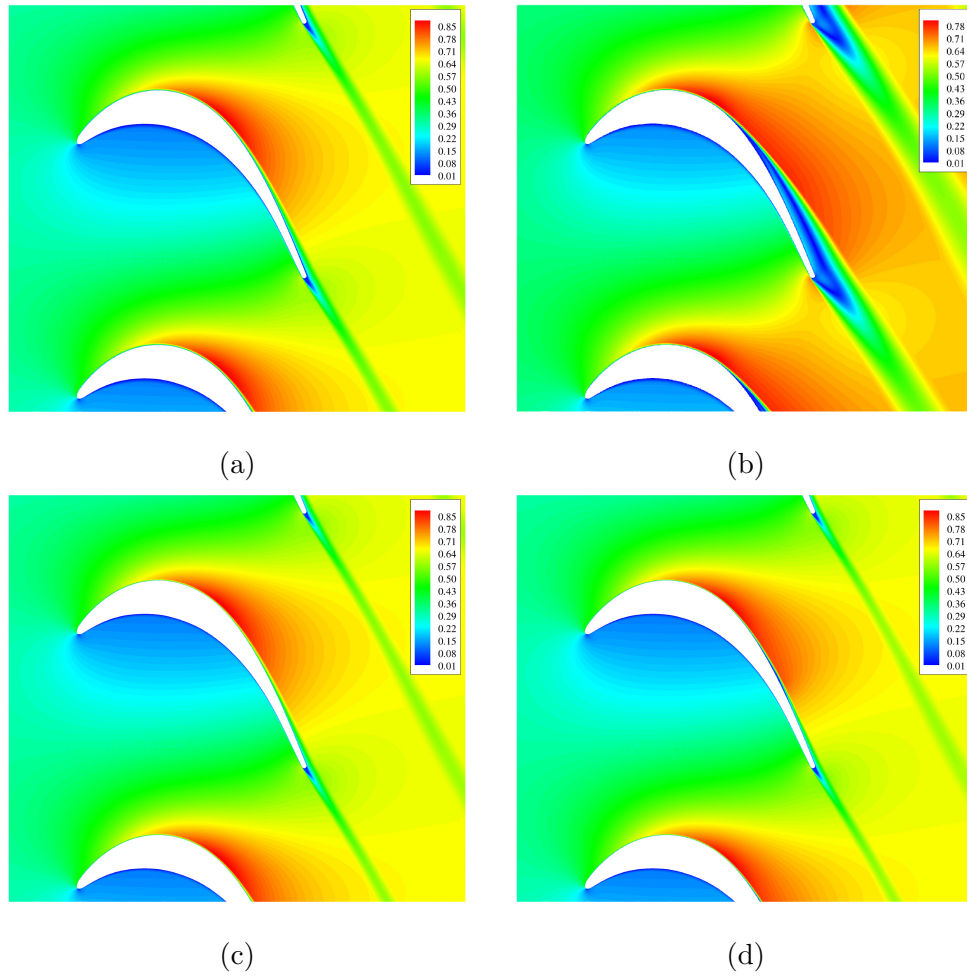


Figure 3: Mach field for T106c with the original SA model (a,c) and with optimised model (b,d) at  $Re_{2s} = 8 \cdot 10^4$  (a,b)  $Re_{2s} = 2.5 \cdot 10^5$  (c,d)

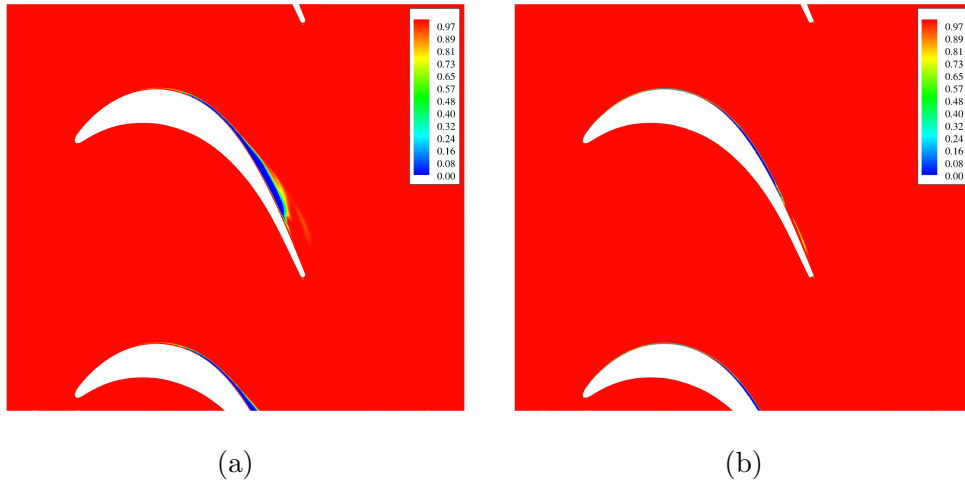


Figure 4: Correction field  $h(x)$  for T106c at  $Re_{2s} = 8 \cdot 10^4$  (a) and  $Re_{2s} = 2.5 \cdot 10^5$  (b) with  $\lambda = 0$

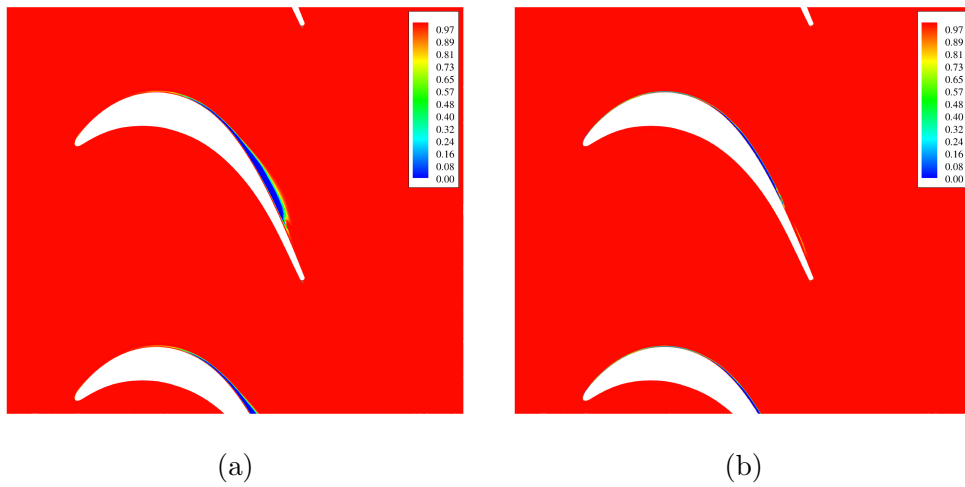


Figure 5: Correction field  $h(x)$  for T106c at  $Re_{2s} = 8 \cdot 10^4$  (a) and  $Re_{2s} = 2.5 \cdot 10^5$  (b) with  $\lambda = 10^{-3}$

401 related to the inputs and the architecture of the ANN used to express the  
402 correction factor will be investigated.

### 403 *6.1. Choice of the inputs*

404 The choice of the input variables of the ANN is not a trivial task. In  
405 particular, it is necessary to avoid input variables which would introduce  
406 a dependency on the particular frame of reference which is used to study  
407 the problem (i.e. Galilean invariance must be satisfied). Furthermore, there  
408 should not be strong correlations between the different input variables and  
409 they should be chosen as adimensional quantities in order to get general re-  
410 sults.

411 A natural choice is to identify some adimensional groups which appear in  
412 the source term of the original RANS model and use them as input for the  
413 ANN. This choice was for example carried out by Singh et al. (44).

414 A similar approach is used in this work but particular attention is here de-  
415 voted to the robustness and the prediction ability of the model. The following  
416 five input variables are used:  $\chi$ ,  $\log(\tau/\tau_{ref} + \epsilon)$ ,  $f'_d$ ,  $\log(P/(D + \epsilon) + \epsilon)$  and  
417  $\log(|\nabla\tilde{\nu}|d/(\nu + \tilde{\nu}) + \epsilon)$ . The plots in Figure 6 show the distribution for all  
418 the inputs variables in the optimised solution at  $Re_{2s} = 8 \cdot 10^4$ .

419

420 The first input,  $\chi$ , simply represents the turbulent intensity. The quantity  
421  $\tau/\tau_{ref}$  is obtained by normalising the module of the stress tensor with respect  
422 to a reference stress. The reference stress is here defined as  $\tau_{ref} = \rho(\nu + \tilde{\nu})^2/d^2$   
423 which makes this input a local quantity. In contrast, Singh et al. (44)  
424 used a non local normalisation in which the stress tensor is normalised with  
425 respect to the wall stress  $\tau_w$ . However, such non-local terms are avoided

426 in this work since the presence of non-local terms reduces significantly the  
 427 scalability of the discretisation in a parallel environment. Furthermore, the  
 428 physical meaning of using  $\tau_w$  for the normalisation is clear for the mesh points  
 429 in the boundary layer but is not so clear for other regions, like for example  
 430 the wake. Finally, a logarithmic scaling of the quantity  $\tau/\tau_{ref}$  was observed  
 431 to significantly improve the fitting of the database. The additive constant  
 432  $\epsilon = 10^{-5}$  is introduced to prevent the algorithm of the logarithm to become  
 433 null.

434 The term  $f'_d$  is introduced in this work as a modification of the term  $f_d$  used  
 435 by Singh et al. (44) and originally proposed by (52) in the framework of  
 436 Detached Eddy Simulations. The terms are defined as:

$$f_d = 1 - \tanh((8r_d)^3) \quad f'_d = 1 - \tanh((r_d)^{0.5}) \quad (24)$$

437 where the quantity  $r_d$  is an adimensional group obtained by combining wall  
 438 distance, turbulence and molecular viscosity and velocity gradient:

$$r_d = \frac{\nu + \tilde{\nu}}{d^2 \kappa^2 \sqrt{\frac{\partial u_i}{\partial x_j} \frac{\partial u_i}{\partial x_j}}} \quad (25)$$

439 where  $\kappa = 0.41$  is the von Karman constant.

440 The plot in Figure 6 explains why in this work the term  $f'_d$  is used instead of  
 441  $f_d$ : both terms are limited between 0 and 1 but  $f'_d$  allows to better describes  
 442 the flow features close to wall while  $f_d$  tends to compress the information  
 443 and does not allow to distinguish the different structures. This qualitative  
 444 analysis was confirmed by quantitative analysis which shows that an ANN  
 445 with  $f'_d$  was able to better fit the database with respect to an equivalent ANN  
 446 with  $f_d$  as input.

447

448 The term  $\log(P/(D + \epsilon) + \epsilon)$  represents a convenient scaling of the ratio  
 449 between the production  $P$  and destruction  $D$  terms of the SA model. In the  
 450 work of Singh et al. (44) the ratio  $P/D$  is directly used while in this work a  
 451 logarithmic scaling is used: this is due to the fact that the values assumed  
 452 by this ratio are distributed in a wide range which covers several orders of  
 453 magnitude and some numerical experiments confirmed that the fitting sig-  
 454 nificantly improves with this scaling. Furthermore, both the numerator and  
 455 the denominator of this quantity can go to zero in the presence of uniform  
 456 fields or where the turbulence viscosity is zero and so the constant  $\epsilon = 10^{-5}$  is  
 457 introduced. Some numerical tests showed that the use of logarithmic scaling  
 458 improves significantly the fitting of the database with the ANN.  
 459 Finally, the adimensional gradient of the modified turbulent viscosity  $\log(|\nabla \tilde{\nu}|d/(\nu +$   
 460  $\tilde{\nu}) + \epsilon)$  is considered. This quantity was not used in (44) and does not appear  
 461 in the production and destruction terms. However, it appears in the cross  
 462 production term (the last term of Eq. 4) and allows to identify regions with  
 463 strong variations in the eddy viscosity. It is normalised with respect to the  
 464 wall distance and the sum of kinematic and eddy viscosity: this means that  
 465 this quantity remains well conditioned even when the eddy viscosity tends  
 466 to zero since the kinematic viscosity prevents the denominator to become  
 467 zero. Even for this variable the logarithmic scaling was found to be useful to  
 468 improve the fitting.

469

## 470 6.2. Choice of the ANN architecture

471 After choosing the input features, it is necessary to define the architec-  
 472 ture of the ANN. In this work, feedforward ANNs are considered. As far as

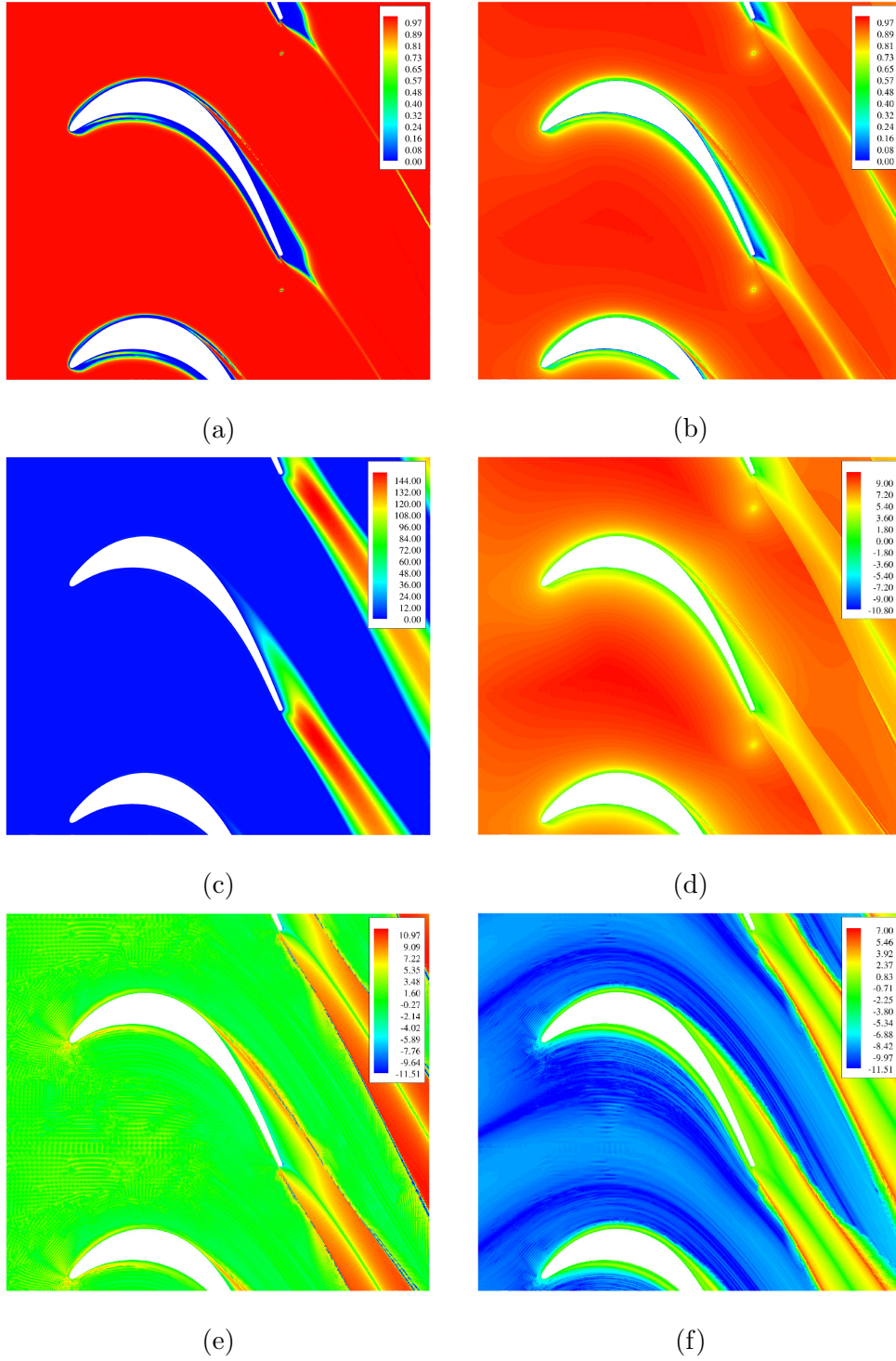


Figure 6: Input features for the neural network:  $f_d$  (a),  $f'_d$  (b),  $\chi$  (c),  $\log(\tau/\tau_{ref} + \epsilon)$  (d),  $\log(P/(D + \epsilon) + \epsilon)$  (e),  $\log(|\nabla \tilde{v}|d/(\nu + \tilde{v}) + \epsilon)$  (f)

473 the activation functions are concerned, a common choice consists in using  
474 sigmoid functions for the hidden layers and linear functions for the output  
475 layer. However, since the chosen correction factor  $h$  is limited in the range  
476  $[0, 1]$  a sigmoid activation function is adopted also for the output layer: in  
477 this way the output of the ANN will be automatically limited in the range  
478  $[0, 1]$  .

479

480 Particular care should be taken in choosing the number of hidden layers  
481  $n_{HL}$  and the number of neurons per layer  $n_N = 10$ . In particular it is  
482 necessary to find a compromise between the complexity of the network (which  
483 allows to capture the correlations hidden in the database) and its ability to  
484 perform predictions outside of the database. When the complexity of the  
485 network is increased its ability to reproduce the training database is enhanced  
486 because it has more degrees of freedom which can be adjusted to fit the data.  
487 However, if too many degrees of freedom are introduced then the network  
488 will behave poorly during predictions: this is due to the fact that when too  
489 many degrees of freedom are used then the output of the network will show  
490 strong oscillations for the points in the parameter space which do not exactly  
491 match a training point.

492 In order to find a suitable network by using a general criteria the following  
493 approach is used. First of all, different architectures are considered ( $1 \leq$   
494  $n_{HL} \leq 25 \leq n_N \leq 40$ ) and the ability of the networks to fit the database is  
495 investigated. Each network is trained in Matlab by means of the Levenberg-  
496 Marquadt algorithm with a goal function based on the mean squared error.  
497 The training is performed by dividing randomly the database in 3 subsets:



498 one for training (70% of the data), one for validation (15% of the data) and  
499 one for test (15% of the data). The training set is actually used for the  
500 computation of the mean square error and for driving the training process.  
501 The validation set is used during the training to verify that the ANN is still  
502 able to give good predictions for points which do not belong to the training  
503 set: when the validation error tends to increase the training is arrested,  
504 even if the training error is still decreasing, in order to limit the problem  
505 of overfitting. Finally, the test set is used to monitor the behaviour of the  
506 ANN on an external set of data which do not influence the training process  
507 (neither in the mean squared error computation nor in the validation checks  
508 for the overfitting). An example of training history is reported in Figure 7a  
509 in which it can be clearly seen that when the training is stopped the training  
510 error was still decreasing but the validation error just started to grow. In  
511 Figure 8 it is possible to see the regression plots for the different data sets:  
512 in each plot the abscissa represents the reference value in the database while  
513 the ordinate represents the approximated value computed by the network.  
514 Another approach for avoiding overfitting was also investigated: Bayesian  
515 regularisation (53). In Bayesian regularisation the mean square error goal  
516 function is augmented by a term which penalises large values of the weights.  
517 However, some experiments on the problems considered in this work showed  
518 that the splitting of the database in training, validation and test sets allows  
519 to achieve a better compromise between fitting and robustness with respect  
520 to the Bayesian regularisation.  
521 A sequence of regression plots (on the full database) for the ANN  $2 \times 5$ ,  
522  $2 \times 10$ ,  $2 \times 20$  and  $2 \times 40$  are reported in Figure 9: as the complexity of

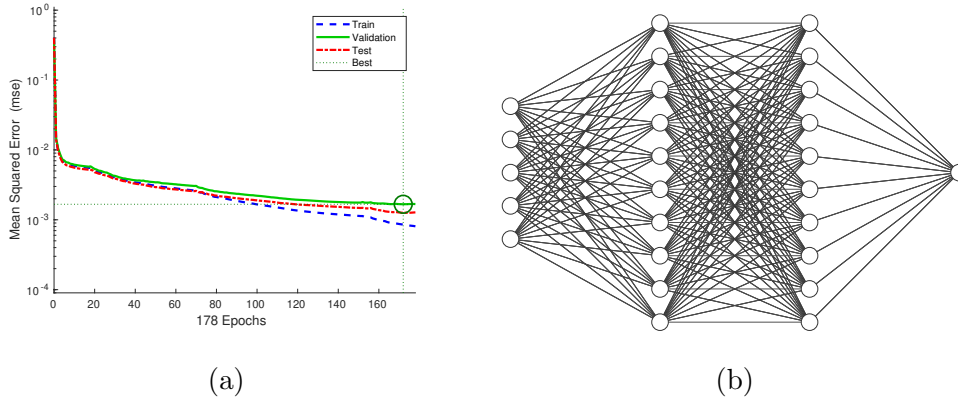


Figure 7: Training history (a) and architecture (b) for 2x20 ANN

523 the network is increased its ability to reproduce the database is enhanced as  
 524 can be clearly seen by the fact that the points tend to assume a distribution  
 525 centered along the bisector of the quadrant.

526 In Table 2 the regression coefficient  $R$  for different ANN architectures are  
 527 reported.

	$n_N = 5$	$n_N = 10$	$n_N = 20$	$n_N = 40$
$n_{HL} = 1$	0.799	0.831	0.865	0.897
$n_{HL} = 2$	0.822	0.890	0.918	0.953

Table 2: Regression coefficient  $R$  for several architectures of the ANN

528 According to the previous analysis it would seem that the larger is the  
 529 network the better is the result. This is true for the fitting of the points  
 530 in the database. However, it is fundamental to investigate the behaviour of  
 531 the network for points which do not coincide exactly with the points in the  
 532 database. In order to do this it is possible to run some CFD simulations at

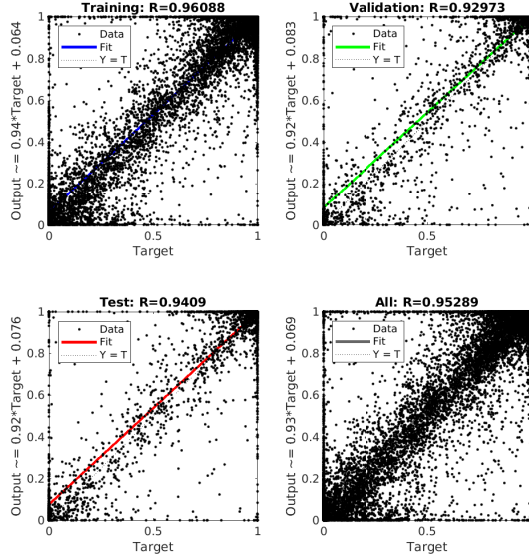
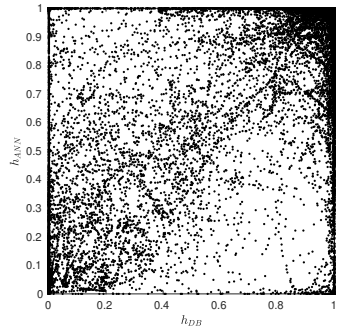
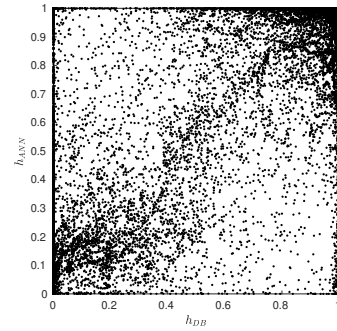


Figure 8: Training, validation and test error for 2x20 ANN

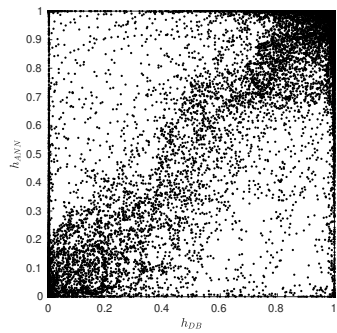
533  $Re_{2s} = 8 \cdot 10^4$  and  $Re_{2s} = 2.5 \cdot 10^5$  with the correction term  $h$  estimated by the  
 534 different ANNs. Apparently, this seems a useless check since the database  
 535 used for the training is built from the optimal solution at these Reynolds  
 536 number and so one could aspect that the ANN should reproduce perfectly  
 537 these working conditions. However, it is important to keep in mind that  
 538 the regression coefficient  $R$  is always less than 1: this means that, even if  
 539 the CFD simulation is initialised with the optimal solution obtained by the  
 540 adjoint approach, the correction field reproduced by the ANN will not co-  
 541 incide exactly which the optimal one. As a consequence, the CFD solution  
 542 will evolve towards a new steady solution. This introduces a perturbation in  
 543 the input features given to the ANN: if the ANN is robust the new steady  
 544 solution will be close to the optimal one. However, if the ANN is poorly



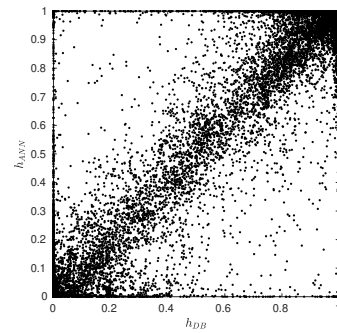
(a)



(b)



(c)



(d)

Figure 9: Regression plots for different ANN architectures: 2x5 (a), 2x10 (b), 2x20 (c), 2x40 (d)

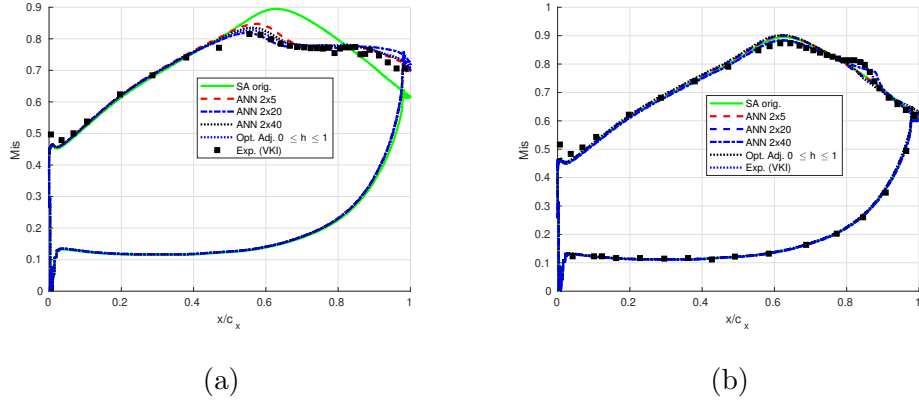


Figure 10: Comparison of different ANN architectures in terms of wall isentropic Mach number distribution on the T106c at  $Re_{2s} = 8 \cdot 10^4$ (a) and  $Re_{2s} = 2.5 \cdot 10^5$ (b):

545 conditioned because an excessive number of neurons has been chosen then  
 546 the network will give a significantly different response.

547 This behaviour was verified by checking the wall isentropic Mach number  
 548 distribution reported in Figure 10 for the ANNs with  $2 \times 5$ ,  $2 \times 10$ ,  $2 \times 20$   
 549 and  $2 \times 40$  neurons. It can be seen that the  $2 \times 5$  network performs poorly  
 550 because of its inability to reproduce the database. The networks with  $2 \times 10$   
 551 and  $2 \times 20$  neurons performs significantly better and gives solutions which  
 552 are very close to the optimal ones. The largest network with  $2 \times 40$  neurons  
 553 starts to show some problems at  $Re_{2s} = 2.5 \cdot 10^5$  in which it is not able to  
 554 reproduce the small separation bubble.

555 According to this analysis, all the predictive simulations reported in the fol-  
 556 lowing will be performed by using the  $2 \times 20$  ANN.

557

558 **7. Predictions**

559 In the previous Section the procedure for choosing the architecture of  
 560 the ANN is reported. Now, the chosen network is use to perform predictive  
 561 simulation for working conditions and geometries which were not included  
 562 in the database. As a first step all the simulations are performed by setting  
 563  $h(x) = 1$ , i.e. with the original SA model. Then the obtained steady solution  
 564 is used to initialise a simulation in which the correction term is computed  
 565 with the ANN. This approach speed ups the convergence since the ANN is  
 566 not employed during the strong initial transient at the beginning of the sim-  
 567 ulation.

568

569 Furthermore, the numerical experiments showed that the robustness of  
 570 the method during predictive simulations can be improved by limiting the  
 571 input variables to the range used for the training. This is important because  
 572 the ANN has been trained only on a few steady solutions and so during  
 573 the transients which can appear in predictive simulations the input features  
 574 could assume values which were not observed in the training database. In  
 575 particular, if  $h(\mathbf{Y})$  represents the ANN approximation of the correction fac-  
 576 tor and  $\mathbf{Y}$  is the vector of the five input variables, the modified expression  
 577  $h(L(\mathbf{Y}))$  is used during predictive simulations, where the limiting function  $L$   
 578 is defined as:

$$L(Y_i) = \begin{cases} Y_i & \text{if } Y_i^{min} \leq Y_i \leq Y_i^{max} \\ Y_i^{max} & \text{if } Y_i > Y_i^{max} \\ Y_i^{min} & \text{if } Y_i < Y_i^{min} \end{cases} \quad (26)$$

579 Here  $Y_i^{min}$  and  $Y_i^{max}$  represent the minimum and maximum values of the i-th

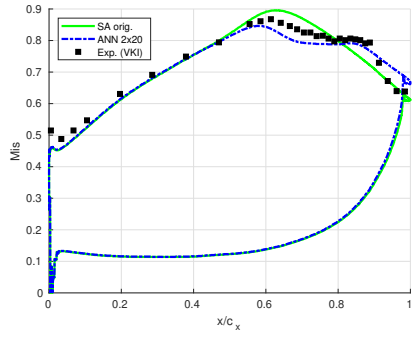
580 input feature observed in the training database.

### 581 *7.1. T106c cascade at different Reynolds number*

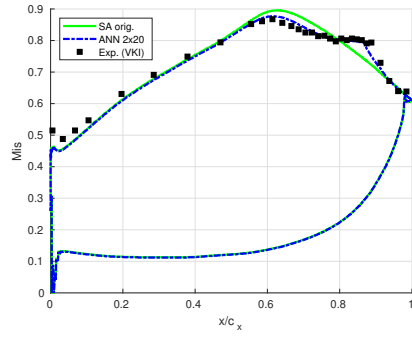
582 As a first test, the ANN augmented SA model is used to predict the flow  
583 field on the T106c at  $Re_{2s} = 1.2 \cdot 10^5$ ,  $1.6 \cdot 10^5$  and  $2.1 \cdot 10^5$ . In this range  
584 of Reynolds number a strong variation is observed in the solution due to the  
585 transition from open to closed separation. The results related to the wall  
586 isentropic Mach number distribution are reported in Figure 11 in which they  
587 are compared with the available experimental results and the original SA  
588 model. The ANN augmented SA model performs significantly better than  
589 the original model and the predictions are quite close to the experiment. Only  
590 the solution obtained at  $Re_{2s} = 1.2 \cdot 10^5$  seems to overpredict the separation.

591 The results reported in Figure 11 refer to the  $M_{is}$  distribution used in the  
592 goal function which drove the field inversion and so it is natural to expect  
593 an improvement with respect to the original model. However, the prediction  
594 ability of the model was also investigated in terms of mass averaged kinetic  
595 losses  $\zeta$  and exit angle  $\beta_2$  in the wake, quantities which were not included in  
596 the goal function used for the optimisation.

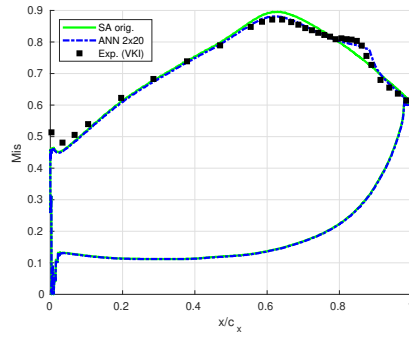
597 The average is performed in a control section located  $0.465c_x$  behind the  
598 trailing edge, where  $c_x$  is the axial chord, in the same location used for the  
599 experimental measurements. The results of these tests are reported in Figure  
600 12. As far as the losses are concerned, both the original SA model and the  
601 ANN augmented SA model perform well for high Reynolds values. However,  
602 for low Reynolds numbers the original SA model misses completely the sepa-  
603 ration and so it underpredicts significantly the losses. The ANN augmented  
604 SA model shows the correct trend and is quite close to the experimental re-



(a)



(b)



(c)

Figure 11: Wall isentropic Mach number distribution: predictions at  $Re_{2s} = 1.2 \cdot 10^5$  (a),  $Re_{2s} = 1.6 \cdot 10^5$  (b) and  $Re_{2s} = 2.1 \cdot 10^5$  (c)



605 sults at  $Re_{2s} = 8 \cdot 10^4$  (for which the optimisation was performed). The plot  
 606 shows also the results obtained by Benyahia et al. (54) with the SST- $\gamma$ - $Re_\theta$   
 607 model based on the correlations proposed by (55), by Pacciani et al.(56) with  
 608 the  $k - \omega$  model coupled with a transport equation for the laminar kinetic  
 609 energy and by Babajee (50) with the SST- $\gamma$ - $Re_\theta$  model (57; 58). The bound-  
 610 ary condition for the turbulent kinetic energy equation which appears in the  
 611 SST model is clearly defined by the experimental inlet turbulence intensity  
 612 (0.9%). However, the SST model requires also an inlet boundary condition  
 613 for the  $\omega$  equation which is usually prescribed by defining an inlet turbulence  
 614 Reynolds number ( $Re_T$ ). Babajee performed a study on the choice of the in-  
 615 let value for  $Re_T$ : in particular he found the optimal value of  $Re_T$  which fits  
 616 the experimental turbulence decay in the wind tunnel without the cascade.  
 617 However, when this value is imposed at the inlet, the SST- $\gamma$ - $Re_\theta$  model is  
 618 not able to predict accurately the separation. For this reason he performed  
 619 a parametric study changing  $Re_T$  in order to match at best the experimen-  
 620 tal results on the T106c. For this reason, the plot shows two set of results  
 621 related to the SST- $\gamma$ - $Re_\theta$  model: the results with the boundary condition  
 622 which is coherent with the physical decay of turbulence in the wind tunnel  
 623 ( $Re_T = TD$ ) and the results with an alternative value which gives better  
 624 predictions ( $Re_T = 0.01$ ).

625 As far as the average exit angle is concerned, the ANN augmented SA model  
 626 shows a better behaviour than the original SA model at low Reynolds num-  
 627 bers while the two models give similar results at higher Reynolds numbers.  
 628 It is interesting to note that the asymptotic value of the exit angle for high  
 629 values of Reynolds number presents an offset between experimental and nu-

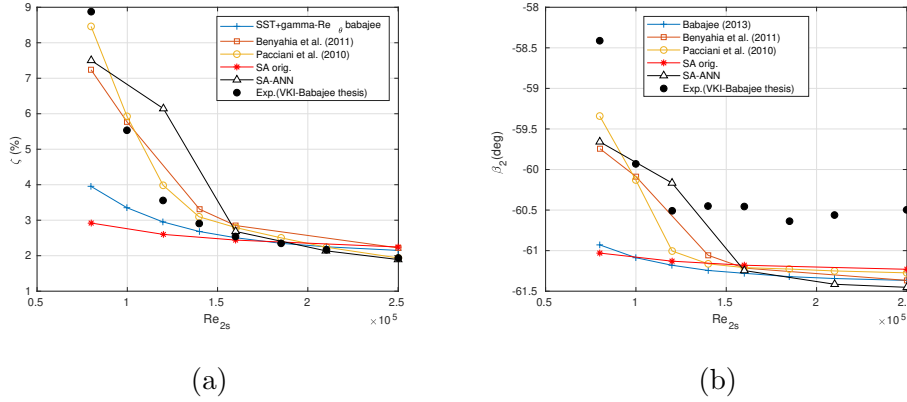


Figure 12: Average losses and exit angle for T106c cascade: comparison between original SA model, SA-ANN model and experimental results

630 merical results. However, this offset was observed also by other results in the  
 631 literature as shown by the SST- $\gamma$ - $Re_\theta$  results from (50).

632

### 633 7.2. T2 cascade

634 The prediction ability of the ANN augmented SA model is investigated  
 635 also on another geometry, the T2 cascade. The simulations are carried out  
 636 with a third order accurate DG scheme on a mesh with 59453 elements, cor-  
 637 responding to 356718 degrees of freedom per equation. The mesh resolution  
 638 at wall and in the wake region is the same used for the T106c, since both  
 639 cascades are investigated at similar values of Reynolds number. The T2  
 640 airfoil was designed at the VKI for the same velocity triangles of the T106  
 641 (inlet angle  $\alpha = 32.7^\circ$ ) but it is characterised by a larger pitch-to-chord ratio  
 642 (1.05) and an increased diffusion rate along the rear suction side (50). Also  
 643 the Zweifel number is larger ( $\Psi = 1.46$ ) with respect to the T106 ( $\Psi = 1.24$ ).  
 644 The isentropic exit Mach number is set to  $M_{2s} = 0.65$ .

645 In Figure 13 and 14 the Mach number field at  $Re_{2s} = 1.2 \cdot 10^5$  and  $2.1 \cdot 10^5$  is  
646 reported for the original SA model and for the ANN augmented SA model.  
647 The plots show clearly the presence of a open separation at  $Re_{2s} = 1.2 \cdot 10^5$   
648 and a closed separation at  $Re_{2s} = 2.1 \cdot 10^5$ .

649 Finally, in Figure 15 the predicted wall isentropic Mach number distribution  
650 is reported as a function of the curvilinear coordinate  $s$  along the blade sur-  
651 face, normalised with respect to the curvilinear length of the blade ( $s_0$ ). The  
652 ANN augmented SA model shows significant improvements with respect to  
653 the baseline SA model and gives good results also with respect to the SST-  
654  $\gamma-Re_\theta$  results from (50).

655 Finally, the models are evaluated in terms of mass averaged exit kinetic losses  
656 and angle, as reported in Figure 16. As observed for the T106c, even in this  
657 case the ANN augmented SA model outperforms the original SA model at  
658 low Reynolds numbers. It is interesting to note that the numerical results  
659 obtained in the present work presents an offset in  $\beta_2$  with respect to the ex-  
660 perimental results, offset which is not observed in the results obtained from  
661 the SST- $\gamma-Re_\theta$  model. This could be a limitation of the SA model which  
662 is inherited by the augmented model: future work will be devoted to apply  
663 the field inversion approach to other RANS models to verify whether this  
664 limitation persists.

## 665 8. Conclusions

666 The potential of the field inversion approach was investigated for the aug-  
667 mentation of a RANS model used in the simulation of turbomachinery flows.  
668 In particular the approach was applied to the original SA model and the

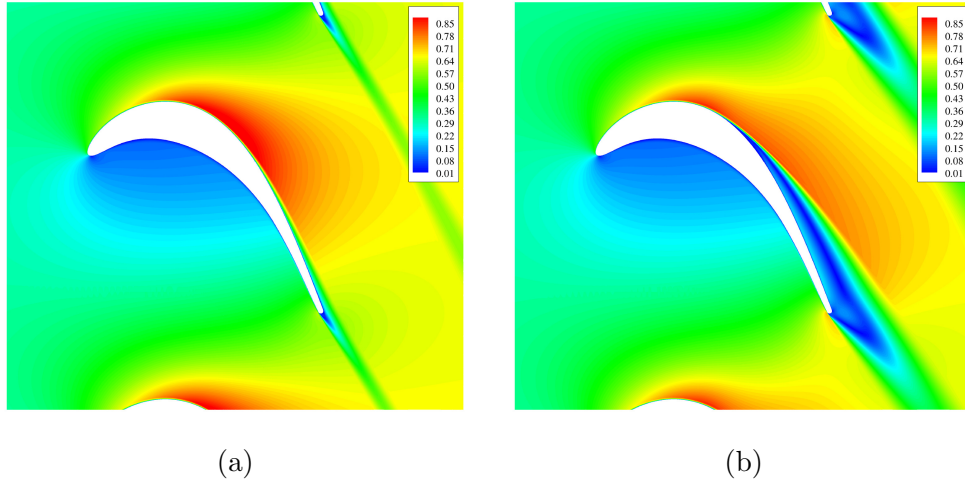


Figure 13: Mach field for the T2 cascade at  $Re_{2s} = 1.2 \cdot 10^5$  with the original SA model (a) and with the ANN-SA model (b)

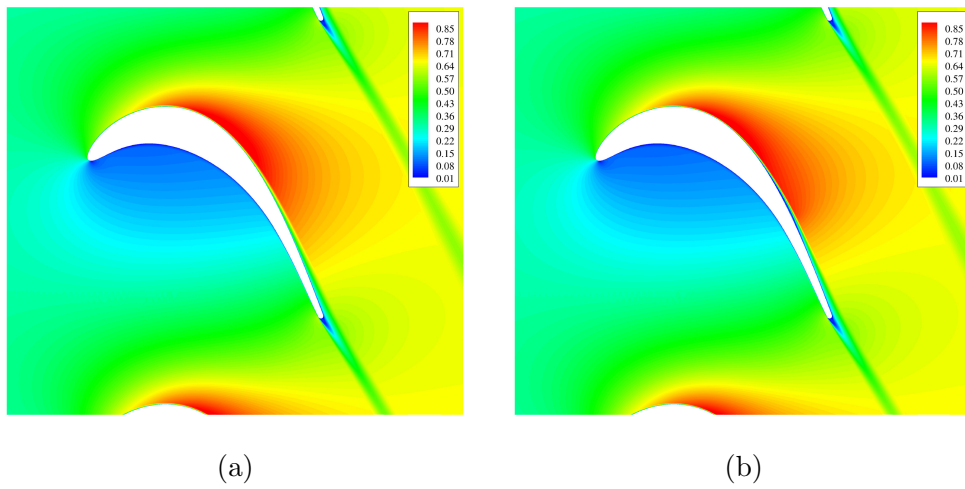


Figure 14: Mach field for the T2 cascade at  $Re_{2s} = 2.1 \cdot 10^5$  with the original SA model (a) and with the ANN-SA model (b)

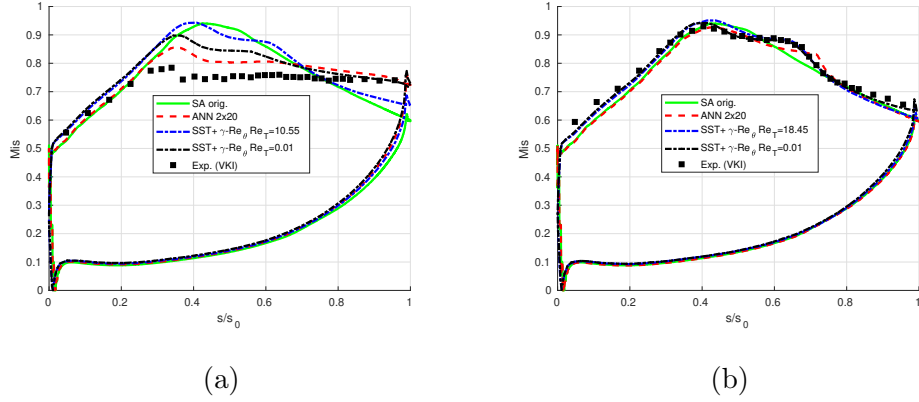


Figure 15: Mis distribution for T2 cascade at  $Re_{2s} = 1.2 \cdot 10^5$ (a) and  $Re_{2s} = 2.1 \cdot 10^5$ (b): comparison between original SA model, SA-ANN model and experimental results

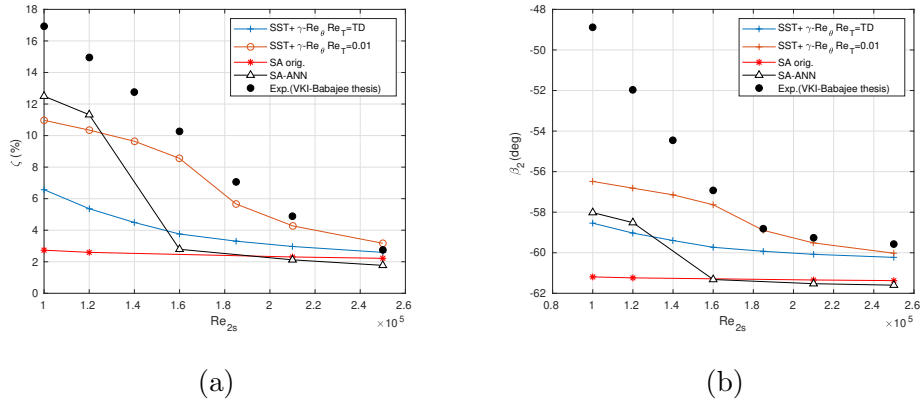


Figure 16: Average losses and exit angle for T2 cascade: comparison between original SA model, SA-ANN model and experimental results

669 attention is focused on transitional flows with separation in low pressure gas  
670 turbines. Since the original model is not suited for this kind of flows, the  
671 field inversion approach is used to develop a local correction of the produc-  
672 tion term which acts like an intermittency correction for transitional flows.  
673 The correction factor is then expressed by means of an ANN as a function  
674 of some physical quantities in order to generalise the model. An investiga-  
675 tion has been carried out on the definition of the input features which are  
676 improved with respect to the original definitions suggested in the literature.  
677 A convergence study is carried out to choose the architecture of the ANN in  
678 order to underline the problem of overfitting. The ability of the ANN aug-  
679 mented SA model to compute low Reynolds number flow fields in low pressure  
680 gas turbine cascades is investigated by performing actual predictions at dif-  
681 ferent Reynolds numbers and on a different geometry with respect to the one  
682 used for the field inversion. Furthermore, a new expression of the correction  
683 term is proposed in order to limit its value in a finite range: this, together  
684 with the introduction of a limiting on input features, significantly improves  
685 the robustness of the approach during transients and in predictions.  
686 The results seem promising and are substantially better than the results pro-  
687 vided by the original model. They also appears satisfactory if compared to  
688 the results obtained by a significantly more complex four equation model  
689 (SST- $\gamma$ - $Re_\theta$ ). In particular, even if the goal function used for the field inver-  
690 sion is based only on the wall isentropic Mach number, the ANN augmented  
691 model shows improvements also in terms of average losses and exit angle in  
692 the wake.  
693 Future work will be devoted to the application of the field inversion approach

694 to other RANS models. Furthermore, possible alternatives to the use of an  
695 ANN will be investigated for achieving a better fitting of the database with  
696 a good level of robustness in predictions.

## 697 **9. Acknowledgements**

698 Computational resources were provided by HPC@POLITO, a project of  
699 Academic Computing within the Department of Control and Computer En-  
700 gineering at the Politecnico di Torino (<http://www.hpc.polito.it>).

701 We acknowledge the CINECA award under the ISCRA initiative, for the avail-  
702 ability of high performance computing resources and support. The simula-  
703 tions were performed on the Marconi Tier-0 System for the Project FIRST.

## 704 **References**

- 705 [1] S. Russo, P. Luchini, A fast algorithm for the estimation of statistical  
706 error in dns (or experimental) time averages, *Journal of Computational*  
707 *Physics* 347 (2017) 328–340.
- 708 [2] R. D. Sandberg, V. Michelassi, The current state of high-fidelity simula-  
709 tions for main gas path turbomachinery components and their industrial  
710 impact, *Flow, Turbulence and Combustion* 102 (4) (2019) 797–848.
- 711 [3] X. Xie, M. Mohebujjaman, L. G. Rebholz, T. Iliescu, Data-driven fil-  
712 tered reduced order modeling of fluid flows, *SIAM Journal on Scientific*  
713 *Computing* 40 (3) (2018) B834–B857.

- 714 [4] R. Dupuis, J.-C. Jouhaud, P. Sagaut, Surrogate modeling of aerody-  
715 namic simulations for multiple operating conditions using machine learn-  
716 ing, *AIAA Journal* 56 (9) (2018) 3622–3635.
- 717 [5] L. Margheri, M. Meldi, M. V. Salvetti, P. Sagaut, Epistemic uncer-  
718 tainties in rans model free coefficients, *Computers & Fluids* 102 (2014)  
719 315–335.
- 720 [6] A. Ferrero, A. Iollo, F. Larocca, Reduced order modelling for turbo-  
721 machinery shape design, *International Journal of Computational Fluid*  
722 *Dynamics* (2019) 1–12.
- 723 [7] A. Ferrero, A. Iollo, F. Larocca, Global and local pod models for the  
724 prediction of compressible flows with dg methods, *International Journal*  
725 *for Numerical Methods in Engineering* 116 (5) (2018) 332–357.
- 726 [8] M. Bergmann, A. Ferrero, A. Iollo, E. Lombardi, A. Scardigli, H. Telib,  
727 A zonal galerkin-free pod model for incompressible flows, *Journal of*  
728 *Computational Physics* 352 (2018) 301–325.
- 729 [9] M. Raissi, G. E. Karniadakis, Hidden physics models: Machine learn-  
730 ing of nonlinear partial differential equations, *Journal of Computational*  
731 *Physics* 357 (2018) 125–141.
- 732 [10] J.-X. Wang, J.-L. Wu, H. Xiao, Physics-informed machine learning ap-  
733 proach for reconstructing reynolds stress modeling discrepancies based  
734 on dns data, *Physical Review Fluids* 2 (3) (2017) 034603.
- 735 [11] J. Weatheritt, R. Sandberg, A novel evolutionary algorithm applied to



- 736 algebraic modifications of the rans stress–strain relationship, *Journal of*  
737 *Computational Physics* 325 (2016) 22–37.
- 738 [12] J. Weatheritt, R. Pichler, R. D. Sandberg, G. Laskowski, V. Michelassi,  
739 Machine learning for turbulence model development using a high-fidelity  
740 hpt cascade simulation, in: *ASME Turbo Expo 2017: Turbomachinery*  
741 *Technical Conference and Exposition*, American Society of Mechanical  
742 Engineers Digital Collection, 2017.
- 743 [13] K. Duraisamy, Z. J. Zhang, A. P. Singh, New approaches in turbulence  
744 and transition modeling using data-driven techniques, in: *53rd AIAA*  
745 *Aerospace Sciences Meeting*, 2015, p. 1284.
- 746 [14] E. J. Parish, K. Duraisamy, A paradigm for data-driven predictive mod-  
747 eling using field inversion and machine learning, *Journal of Computa-*  
748 *tional Physics* 305 (2016) 758–774.
- 749 [15] F. Gibou, D. Hyde, R. Fedkiw, Sharp interface approaches and deep  
750 learning techniques for multiphase flows, *Journal of Computational*  
751 *Physics* 380 (2019) 442–463.
- 752 [16] H. Patel, A. Panda, J. Kuipers, E. Peters, Computing interface curva-  
753 ture from volume fractions: A machine learning approach, *Computers*  
754 *& Fluids* 193 (2019) 104263.
- 755 [17] A. Takbiri-Borujeni, M. Ayoobi, Application of physics-based machine  
756 learning in combustion modeling (2019).
- 757 [18] S. Bhalla, M. Yao, J.-P. Hickey, M. Crowley, Compact representation of

- 758 a multi-dimensional combustion manifold using deep neural networks,  
759 in: European Conference on Machine Learning, 2019.
- 760 [19] X. Zhu, Z. Cai, J. Wu, Y. Cheng, Q. Huang, Convolutional neural net-  
761 work based combustion mode classification for condition monitoring in  
762 the supersonic combustor, *Acta Astronautica* 159 (2019) 349–357.
- 763 [20] Y.-P. Zhao, Q.-K. Hu, J.-G. Xu, B. Li, G. Huang, Y.-T. Pan, A robust  
764 extreme learning machine for modeling a small-scale turbojet engine,  
765 *Applied energy* 218 (2018) 22–35.
- 766 [21] Z. Liu, I. A. Karimi, Gas turbine performance prediction via machine  
767 learning, *Energy* (2019) 116627.
- 768 [22] K. Duraisamy, G. Iaccarino, H. Xiao, Turbulence modeling in the age of  
769 data, *Annual Review of Fluid Mechanics* 51 (2019) 357–377.
- 770 [23] S. R. Allmaras, F. T. Johnson, Modifications and clarifications for the  
771 implementation of the spalart-allmaras turbulence model, in: Seventh  
772 international conference on computational fluid dynamics (ICCFD7),  
773 2012, pp. 1–11.
- 774 [24] A. Ferrero, A. Iollo, F. Larocca, Rans closure by artificial neural net-  
775 works, in: 13 th European Conference on Turbomachinery Fluid dy-  
776 namics & Thermodynamics, EUROPEAN TURBOMACHINERY SO-  
777 CIETY, 2019.
- 778 [25] R. Hartmann, P. Houston, Adaptive discontinuous galerkin finite ele-  
779 ment methods for the compressible euler equations, *Journal of Compu-  
780 tational Physics* 183 (2) (2002) 508–532.

- 781 [26] J.-F. Remacle, J. E. Flaherty, M. S. Shephard, An adaptive discontinu-  
782 ous galerkin technique with an orthogonal basis applied to compressible  
783 flow problems, *SIAM review* 45 (1) (2003) 53–72.
- 784 [27] G. Zenoni, T. Leicht, A. Colombo, L. Botti, An agglomeration-based  
785 adaptive discontinuous galerkin method for compressible flows, *International  
786 Journal for Numerical Methods in Fluids* 85 (8) (2017) 465–483.
- 787 [28] A. Ferrero, F. Larocca, V. Bernaschek, Unstructured discretisation of a  
788 non-local transition model for turbomachinery flows, *Advances in air-  
789 craft and spacecraft science* 4 (5) (2017) 555–571.
- 790 [29] A. Burbeau, P. Sagaut, A dynamic p-adaptive discontinuous galerkin  
791 method for viscous flow with shocks, *Computers & fluids* 34 (4-5) (2005)  
792 401–417.
- 793 [30] G. Giorgiani, S. Fernández-Méndez, A. Huerta, Hybridizable discontin-  
794 uous galerkin p-adaptivity for wave propagation problems, *International  
795 Journal for Numerical Methods in Fluids* 72 (12) (2013) 1244–1262.
- 796 [31] E. Ampellio, F. Bertini, A. Ferrero, F. Larocca, L. Vassio, Turboma-  
797 chinery design by a swarm-based optimization method coupled with a  
798 cfd solver, *Advances in aircraft and spacecraft science* 3 (2) (2016) 149.
- 799 [32] C. Eskilsson, An hp-adaptive discontinuous galerkin method for shal-  
800 low water flows, *International Journal for Numerical Methods in Fluids*  
801 67 (11) (2011) 1605–1623.
- 802 [33] A. Ferrero, F. Larocca, Adaptive cfd schemes for aerospace propulsion,

- 803 in: Journal of Physics: Conference Series, Vol. 841, IOP Publishing,  
804 2017, p. 012017.
- 805 [34] N. Chalmers, G. Agbaglah, M. Chrust, C. Mavriplis, A parallel hp-  
806 adaptive high order discontinuous galerkin method for the incompress-  
807 ible navier-stokes equations, Journal of Computational Physics: X 2  
808 (2019) 100023.
- 809 [35] C. Geuzaine, J.-F. Remacle, Gmsh: A 3-d finite element mesh generator  
810 with built-in pre-and post-processing facilities, International journal for  
811 numerical methods in engineering 79 (11) (2009) 1309–1331.
- 812 [36] M. Lange, M. G. Knepley, G. J. Gorman, Flexible, scalable mesh and  
813 data management using petsc dmpex, in: Proceedings of the 3rd Inter-  
814 national Conference on Exascale Applications and Software, University  
815 of Edinburgh, 2015, pp. 71–76.
- 816 [37] S. Balay, S. Abhyankar, M. Adams, J. Brown, P. Brune, K. Buschelman,  
817 L. Dalcin, A. Dener, V. Eijkhout, W. Gropp, et al., Petsc users manual  
818 (2019).
- 819 [38] F. Bassi, L. Botti, A. Colombo, D. A. Di Pietro, P. Tesini, On the  
820 flexibility of agglomeration based physical space discontinuous galerkin  
821 discretizations, Journal of Computational Physics 231 (1) (2012) 45–65.
- 822 [39] S. Osher, F. Solomon, Upwind difference schemes for hyperbolic systems  
823 of conservation laws, Mathematics of computation 38 (158) (1982) 339–  
824 374.

- 825 [40] M. Pandolfi, A contribution to the numerical prediction of unsteady  
826 flows, *AIAA journal* 22 (5) (1984) 602–610.
- 827 [41] A. Ferrero, F. Larocca, G. Puppo, A robust and adaptive recovery-based  
828 discontinuous galerkin method for the numerical solution of convection–  
829 diffusion equations, *International Journal for Numerical Methods in Flu-*  
830 *ids* 77 (2) (2015) 63–91.
- 831 [42] F. Bassi, L. Botti, A. Colombo, A. Crivellini, N. Franchina, A. Ghi-  
832 doni, S. Rebay, Very high-order accurate discontinuous galerkin com-  
833 putation of transonic turbulent flows on aeronautical configurations,  
834 in: *ADIGMA-A European Initiative on the Development of Adaptive*  
835 *Higher-Order Variational Methods for Aerospace Applications*, Springer,  
836 2010, pp. 25–38.
- 837 [43] A. Ferrero, F. Larocca, Feedback filtering in discontinuous galerkin  
838 methods for euler equations, *Progress in Computational Fluid Dynam-*  
839 *ics, an International Journal* 16 (1) (2016) 14–25.
- 840 [44] A. P. Singh, S. Medida, K. Duraisamy, Machine-learning-augmented pre-  
841 dictive modeling of turbulent separated flows over airfoils, *AIAA Journal*  
842 (2017) 2215–2227.
- 843 [45] C. M. Bishop, Training with noise is equivalent to tikhonov regulariza-  
844 tion, *Neural computation* 7 (1) (1995) 108–116.
- 845 [46] L. Hascoet, V. Pascual, The tapenade automatic differentiation tool:  
846 Principles, model, and specification, *ACM Transactions on Mathemati-*  
847 *cal Software (TOMS)* 39 (3) (2013) 20.

- 848 [47] K. Duraisamy, P. Durbin, Transition modeling using data driven ap-  
849 proaches, in: CTR Summer Program, 2014, p. 427.
- 850 [48] J. Michalek, M. Monaldi, T. Arts, Aerodynamic performance of a very  
851 high lift low pressure turbine airfoil (t106c) at low reynolds and high  
852 mach number with effect of free stream turbulence intensity, Journal of  
853 Turbomachinery 134 (6) (2012) 061009.
- [49] 2nd international workshop on high-order cfd method,  
[https://www.dlr.de/as/desktopdefault.aspx/tabid-8170/13999\\_ead-  
35550/](https://www.dlr.de/as/desktopdefault.aspx/tabid-8170/13999_ead-35550/), *accessed* : 2019 – 12 – 02.
- 854 [50] J. Babajee, Detailed numerical characterization of the separation-  
855 induced transition, including bursting, in a low-pressure turbine envi-  
856 ronment, Ph.D. thesis (2013).
- 857 [51] J. Hourmouziadis, Aerodynamic design of low pressure turbines,  
858 AGARD, Blading Design for Axial Turbomachines 40 p(SEE N 89-27661  
859 22-07) (1989).
- 860 [52] P. R. Spalart, S. Deck, M. L. Shur, K. D. Squires, M. K. Strelets,  
861 A. Travin, A new version of detached-eddy simulation, resistant to am-  
862 biguous grid densities, Theoretical and computational fluid dynamics  
863 20 (3) (2006) 181.
- 864 [53] F. D. Foresee, M. T. Hagan, Gauss-newton approximation to bayesian  
865 learning, in: Proceedings of International Conference on Neural Net-  
866 works (ICNN'97), Vol. 3, IEEE, 1997, pp. 1930–1935.

- 867 [54] A. Benyahia, L. Castillon, R. Houdeville, Prediction of separation-  
868 induced transition on high lift low pressure turbine blade, in: ASME  
869 2011 Turbo Expo: Turbine Technical Conference and Exposition, Amer-  
870 ican Society of Mechanical Engineers Digital Collection, 2011, pp. 1835–  
871 1846.
- 872 [55] C. Content, R. Houdeville, Application of the  $\gamma$ - $r\theta$  laminar-turbulent  
873 transition model in navier-stokes computations, in: 40th Fluid Dynamics  
874 Conference and Exhibit, 2010, p. 4445.
- 875 [56] R. Pacciani, M. Marconcini, A. Arnone, F. Bertini, A cfd study of low  
876 reynolds number flow in high lift cascades, in: ASME Turbo Expo 2010:  
877 Power for Land, Sea, and Air, American Society of Mechanical Engineers  
878 Digital Collection, 2010, pp. 1525–1534.
- 879 [57] F. R. Menter, R. B. Langtry, S. Likki, Y. Suzen, P. Huang, S. Völker, A  
880 correlation-based transition model using local variables—part i: model  
881 formulation, *Journal of turbomachinery* 128 (3) (2006) 413–422.
- 882 [58] R. B. Langtry, F. Menter, S. Likki, Y. Suzen, P. Huang, S. Völker, A  
883 correlation-based transition model using local variables—part ii: test  
884 cases and industrial applications, *Journal of Turbomachinery* 128 (3)  
885 (2006) 423–434.